Production of a highly degenerate Fermi gas of metastable ^{3}He atoms

Kieran F. Thomas, Zhuoxian Ou, Bryce M. Henson, Angela A. Baiju, Sean S. Hodgman, and Andrew G. Truscott
Department of Quantum Science and Technology, Research School of Physics, The Australian National University, Canberra ACT 2601, Australia

(Received 17 November 2022; accepted 21 February 2023; published 15 March 2023)

We report on the achievement of quantum degeneracy in both components of a Bose-Fermi mixture of metastable helium atoms, ^{4}He* and ^{3}He*. Degeneracy is achieved via Doppler cooling and forced evaporation for ^{4}He*, and sympathetically cooling ^{3}He* with ^{4}He*. We discuss our modified implementation, along with the high versatility of our system. This technique is able to produce a degenerate Fermi gas with a minimum reduced temperature of $T/T_F = 0.14(1)$, consisting of 2.5×10^4 ^{3}He* atoms. Due to the high internal energy of both isotopes single atom detection is possible, opening the possibility of a large number of experiments into Bose-Fermi mixtures.

DOI: 10.1103/PhysRevA.107.033313

I. INTRODUCTION

Since the first realization of Bose-Einstein condensation (BEC) in trapped atomic clouds in 1995 [1], BECs have provided a great range of experimental possibilities, such as atom optics [2], the study of the interaction between light and matter [3], and quantum computation [4,5]. This is because they offer a great degree of control and ease of measurement in a large quantum system. Like bosons, ultracold fermions also offer insights into numerous quantum phenomena, for example high-temperature superconductivity [6], and fermionic superfluidity [7,8], and have hence been an active field of experimental study in recent years [9,10]. Furthermore, degenerate Bose-Fermi mixtures have provided access to an even wider array of possible physics, such as phase separation [11–13], and polaron physics [14,15]. While there have been a number of successful investigations into degenerate Fermi gases (DFGs) and Bose-Fermi mixture [16–21], these investigations are generally less common compared to the pure bosonic counterparts. This is primarily due to the increased experimental complexity that fermionic gases bring, as the evaporative cooling that has allowed access to these ultracold temperatures is not directly possible for a single species of polarized fermions. To circumvent this issue the fermionic species is often cooled to degeneracy sympathetically with either another fermionic species [16,22,23], such as a spin mixture of the same atom, or a bosonic one [21,24], as presented in this paper.

Metastable helium (referring to ^{4}He* or ^{3}He* in their respective $2\,^3S_1$ excited electronic states) provides an especially unique platform for the study of dilute quantum gases due to its high internal energy, allowing for efficient single atom detection (for either isotope). This gives access to the quantum many-body wave function via measurements of momentum correlations in the time-of-flight profiles, and thus can be used to test many important questions in the field. For example, ^{4}He* has been used to observe atomic analogs of quantum optics phenomena such as Hanbury Brown–Twiss bunching [2,25], and wavelike interference in atomic systems [26–28], as well as precision tests of quantum electrodynamics [3,29,30].

Being able to detect individual atoms of a Bose-Fermi mixture in the far field will also open the possibility of a range of experiments such as the interplay of the two statistics, the production and measurement of a mass entangled state for quantum tests of gravity [31], and high precision spectroscopic measurements of each isotope allowing for precision test of quantum theory [30]. In this paper, we report on the production of a degenerate Bose-Fermi mixture of bosonic helium (^{4}He*) and fermionic helium (^{3}He*). This is only the second experimental realization of such a mixture, with the first realization achieved by McNamara *et al.* [21], an apparatus which has produced a number of pioneering results [2,29,32]. Following laser cooling of both species, the bosons are first cooled evaporatively and then used as a sympathetic coolant for the fermions. The achievable temperatures relative to their respective critical temperatures and number of atoms are presented and analyzed. We describe our approach of modifying our existing apparatus for the cooling and trapping of ^{4}He* [33] to accommodate ^{3}He* with minimal alterations to the vacuum and laser system. This represents a simplification over the previous experimental realization of McNamara *et al.* [21], which required the implementation of new atom optic elements to incorporate the cooling laser necessary for ^{3}He*. This system is capable of demonstrating and studying many-body correlations and could shed light on some of the most interesting problems in modern quantum physics.

II. BACKGROUND

In this section we will cover the theoretical basis of the cooling techniques applied to both ^{3}He* and ^{4}He*, highlighting the most pertinent distinctions between the two species

(arising primarily from differing electronic structures and masses).

A. Degeneracy temperature for bosonic and fermionic matter

From their respective symmetries under particle exchange we find the behavior of bosons (symmetric) and fermions (antisymmetric) are governed by Bose-Einstein statistics and Fermi-Dirac statistics respectively. At high temperature, quantum statistics become negligible and both of these kinds of particles obey the classical Maxwell-Boltzmann distribution. However, for both fermions and bosons we can define a respective temperature below which quantum effects become apparent, and thus starkly different behavior is displayed both between one another and their classical counterparts.

For the bosons, below the condensation temperature T_C, a macroscopic fraction of the total number of particles will occupy the lowest-energy single-particle state, forming a BEC. If we have N_b bosons in a harmonic trap then the phase transition temperature T_C can be obtained as [34]

$$k_B T_C = 0.94\ \hbar\bar{\omega}_b N_b^{1/3} \tag{1}$$

where k_B is Boltzmann's constant, and $\bar{\omega}_b$ is the geometric mean of the bosons' trapping frequencies.

In contrast, for fermionic matter the Pauli exclusion principle prevents the simultaneous occupation of the same state by two fermions. As a consequence, at low temperature, every fermion settles into the lowest available energy state, successively filling them and forming a Fermi sea. The energy of the highest filled state is called the Fermi energy (E_F) and the corresponding temperature for this energy is the Fermi temperature $k_B T_F = E_F$. For a Fermi gas containing N_f particles in a harmonic trap we have the following expression for T_F [34]:

$$k_B T_F = 1.82\hbar\bar{\omega}_f N_f^{1/3}, \tag{2}$$

where $\bar{\omega}_f$ is the geometric mean of the fermions' trapping frequencies.

We will refer to T/T_F and T/T_C as the reduced temperatures of the Fermi and Bose gases respectively. It is of relevance to note that for our experiment the masses and magnetic moments of ^{3}He* and ^{4}He* give a fixed ratio of the trapping frequencies $\bar{\omega}_f = \sqrt{\frac{4}{3}}\bar{\omega}_b$ and hence

$$T_F = 2.23\left(\frac{N_f}{N_b}\right)^{1/3} T_C. \tag{3}$$

B. Momentum and time-of-flight distributions

We analyze our Bose-Fermi mixture by measuring the time-of-flight profiles of each species on a microchannel plate and delay line detector, which gives the position and time of each atom that strikes it (as described in Sec. III D). In this section we will summarize the analytical forms of the time-of-flight and momentum profiles for both bosons and fermions. While the fermions' distribution can be completely described by a Fermi-Dirac statistics, the distribution of the bosons has two separate components, a BEC and noncondensed part which follows Bose-Einstein statistics. We will approximate this noncondensed component as thermal, and it will hence serve as our thermometer for the system.

The time-of-flight expansion of a BEC has been investigated by Castin and Dum [35], and was found to be well approximated by a rescaling of the in trap density profile. If we have a cylindrical trap $\omega_x \ll \omega_y$, ω_z and $\omega_y = \omega_z = \omega_\perp$, we can solve for the long-time, $\omega_\perp t \gg 1$ where t is the expansion time, time-of-flight profile of the BEC for a harmonic potential:

$$n_b^{\mathrm{TOF}}(x, y, z, t) = \begin{cases} \frac{\mu_b}{g_b}\left(1 - \sum_{d=x,y,z} \frac{r_d^2}{R_d(t)^2}\right), & r_d < R_d \\ 0, & \text{otherwise} \end{cases} \tag{4}$$

where μ_b is the boson chemical potential, $g_b = \frac{4\pi\hbar^2 a_{44}}{m_b}$ is the interaction coefficient between bosons with $a_{44} = 7.512(5)$ nm the ^{4}He* - ^{4}He* scattering length in the $m_J = +1$ state [36], $R_{y,z}(t) = \sqrt{\frac{2\mu_b}{m_b}}t$, and $R_x(t) = \frac{\omega_x}{\omega_\perp}\frac{\pi}{2}\sqrt{\frac{2\mu_b}{m_b}}t$. Note that the time-of-flight profile of a BEC does not ballistically map to its momentum profile [37], as is the case for the Fermi-Dirac and Maxwell-Boltzmann gases. Hence, generally the BEC profile alone does not encode any information on the temperature of the system.

To determine the density distribution of the trapped cloud of fermions we take the semiclassical approximation (also known as the Thomas-Fermi approximation) [38]. In this approximation each fermion is treated as having a definite position and momentum. If we neglect interactions between the fermions due to the suppression of s-wave scattering of identical fermions, the ground-state momentum density profile is given in this approximation by [39]

$$n_f(p) = \frac{1}{(2\pi)^3}\int d^3\vec{r}\, w(\vec{r}, \vec{p}) \tag{5}$$

$$= -A_f \mathrm{Li}_{3/2}\left[-\xi \exp\left(-\frac{|\vec{p}|^2}{2m_f k_B T}\right)\right] \tag{6}$$

where $\xi = e^{\frac{\mu_f}{k_B T}}$ is the fugacity, $A_f = \frac{1}{(2\pi)^{3/2}\hbar^3}(\frac{k_B T}{m\bar{\omega}_f^2})^{3/2}$, and Li_n is the polylogarithmic function of order n.

At high momentum both the fermion and noncondensed boson distributions are well approximated by a classical Maxwell Boltzmann distribution

$$n_t(p) = A_t e^{-\frac{p^2}{2mk_B T}}, \tag{7}$$

where $A_t = \frac{N_t}{(2\pi)^{3/2}(mk_B T)^{3/2}}$, for a given number of thermal particles N_t at a temperature T.

As we can neglect interactions in the fermionic and thermal components, the momentum distribution can be converted to the far-field time-of-flight profiles using the procedure described in Yavin *et al.* [40]. To represent the coordinates of our measurement procedure we will assume our detector is along the x-y plane, with the origin of the plane directly beneath the initial position of the cloud. Hence, the coordinates (x, y, t) correspond to an atom arriving at the detector at time t at the spatial location (x, y) on the detector. First we transform the momenta (p_x, p_y, p_z) into time-of-flight coordinates (x, y, t)

TABLE I. Summary of the momentum and time-of-flight profiles for different particle statistics and a Bose-Einstein condensate. We have used the following abbreviations: p is the magnitude of the three-dimensional momentum vector; $v_{b,f} = (\frac{2k_BT}{m_{b,f}})^{1/2}$ is the most probable velocity of thermal bosons and fermions respectively; $A_{b,f} = \frac{1}{(2\pi)^{3/2}\hbar^3}(\frac{k_BT}{m_{b,f}\bar{\omega}_{b,f}^2})^{3/2}$, $A_t = \frac{N_t}{(2\pi)^{3/2}(mk_BT)^{3/2}}$, and $A_{\mathrm{BEC}} = \frac{\pi\mu_b^2}{m_b}$ are the normalization constants of the respective momentum distributions; $\xi_{f,b} = e^{\frac{-\mu_{f,b}}{k_BT}}$ is the fugacity of the respective distribution; $\lambda = \frac{\pi\omega_x}{2\omega_\perp}$ is the aspect ratio of the time-of-flight profile of the BEC [35]; $R(t) = \sqrt{\frac{2\mu_b}{m_b}}t$; $g(t) = \exp(-\frac{g(t^2-t_0^2)^2}{2v^2t^2})$; $f(x) = \exp(-\frac{x^2}{v^2t_0^2})$. These distributions are all valid for $v_{f,b}t_0 \ll l_0$. This is equivalent to assuming the average expansion of the cloud is negligible compared to the fall distance, which for our experiment is a very good approximation. We use the semiclassical approach and assume the behavior of an ideal gas for all distributions except the BEC. For the BEC, where the mean-field energy dominates we use the scaling solution derived in Ref. [35].

Statistics	In-trap momentum distribution	$n^{\mathrm{TOF}}(t)$	$n^{\mathrm{TOF}}(x)$
Bose-Einstein	$A_b\mathrm{Li}_{\frac{3}{2}}[\xi_b\exp(-\frac{p^2}{m_b^2v_f^2})]$	$\pi m_b^3A_bv_b^2g(1+\frac{t_0^2}{t^2})\mathrm{Li}_{\frac{5}{2}}[\xi_bg(t)]$	$\pi m_b^3A_b\frac{v_b^2}{t_0}\mathrm{Li}_{\frac{5}{2}}[\xi_bf(x)]$
Fermi-Dirac	$-A_f\mathrm{Li}_{\frac{3}{2}}[-\xi_f\exp(-\frac{p^2}{m_f^2v_b^2})]$	$-\pi m_f^3A_fv_f^2g(1+\frac{t_0^2}{t^2})\mathrm{Li}_{\frac{5}{2}}[-\xi_fg(t)]$	$-\pi m_f^3A_f\frac{v_f^2}{t_0}\mathrm{Li}_{\frac{5}{2}}[-\xi_ff(x)]$
Maxwell-Boltzmann	$A_te^{-\frac{p^2}{m^2v^2}}$	$\pi m_f^3A_tv^2g(1+\frac{t_0^2}{t^2})g(t)$	$\pi A_tm_f^3\frac{v^2}{t_0}f(x)$
Bose-Einstein Condensate		$\lambda A_{\mathrm{BEC}}t^2[1-(\frac{(g(t^2-t_0^2)}{2R(t)})^2]$	$A_{\mathrm{BEC}}t_0^2[1-(\frac{x}{\lambda R(t_0)})^2]$

via the equations for a ballistic motion under gravity:

$$(p_x, p_y, p_z) \mapsto m \times \left(\frac{x}{t}, \frac{y}{t}, \frac{g(t^2-t_0^2)}{2t}\right), \tag{8}$$

where $t_0 = \sqrt{2l_0/g}$ is the fall time for a zero momentum particle, l_0 is the distance from the center of the trapped cloud to the detector, and g is the acceleration due to gravity. We must also account for the change in differential volume between the two coordinate systems by multiplying the probability density by the relevant Jacobian $J = m_{f,b}^3\frac{gt^2+2l_0}{2t^4}$ [40]. Assuming the initial cloud can be treated as a point source, i.e., the spatial distribution can be ignored, the probability density distributions are related by

$$n^{\mathrm{TOF}}(x,y,t) = m_{f,b}^3\frac{gt^2+2l_0}{2t^4}n\left(\frac{x}{t}, \frac{y}{t}, \frac{g(t^2-t_0^2)}{2t}\right), \tag{9}$$

where $n(p_x, p_y, p_z)$ is the corresponding in trap momentum distribution.

To simplify the fitting process we integrate out two of the time-of-flight dimensions. Explicitly this can be written as

$$n^{\mathrm{TOF}}(t) = \int_{-\infty}^{\infty}\int_{-\infty}^{\infty} dx\,dy\,n_f^{\mathrm{TOF}}(x,y,t), \tag{10}$$

$$n^{\mathrm{TOF}}(x) = \int_0^{\infty} dt\int_{-\infty}^{\infty} dy\,n_f^{\mathrm{TOF}}(x,y,t). \tag{11}$$

The relevant momentum distributions, along with corresponding integrated time-of-flight profiles, are displayed in Table I. Note that while the momentum profiles, and consequently the time-of-flight profiles, for the bosons and fermions look superficially similar their behavior is quite different, most relevantly in how rapidly their high momentum wings decay to a thermal distribution [41].

C. Laser trapping and cooling of ^{3}He* and ^{4}He*

To achieve quantum degeneracy in our Bose-Fermi mixture of He* atoms we apply a series of laser cooling and trapping techniques to both ^{4}He* and ^{3}He* in the $2\,^3S_1$ state simultaneously. The $2\,^3S_1$ state is a metastable state, with a lifetime of 7870(510) s for the ^{4}He* isotope [43], and can therefore be treated as an effective ground state. The lifetime of the $2\,^3S_1$ state in ^{3}He* is expected to be similar. From this state, the laser (Doppler) cooling transitions utilized in our experiment are the D_2: $2\,^3S_1$ $(J=1) \rightarrow 2\,^3P_2$ $(J=2)$ transition in ^{4}He* and the C_3: $2\,^3S_1$ $(F=3/2) \rightarrow 2\,^3P_2$ $(F=5/2)$ transition in ^{3}He*, as highlighted in Fig. 1, which are the same cooling transitions utilized in Ref. [21]. The Doppler cooling limit for both of these transitions is ≈39 μK [48], and simultaneous one-dimensional (1D) Doppler cooling of both isotopes has achieved temperatures of 0.13 mK with no atom loss, which

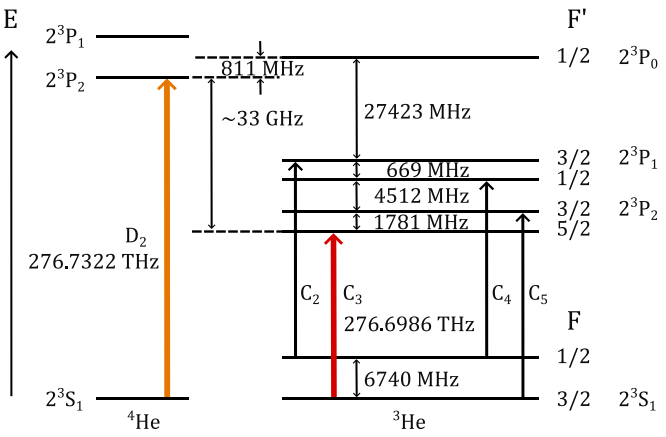

FIG. 1. Energy-level diagrams of ^{4}He* and ^{3}He* relative to the metastable state energy. The spacing of energy levels is only indicative. The $2\,^3S_1$ state of ^{4}He* has a lifetime of 7870(510) s [43]. The D_2 and C_3 atomic transitions for laser cooling and trapping are indicated in orange and red respectively. The resonant frequencies of these two transitions are 276.7322 THz (1083.331 nm) [44] and 276.6986 THz (1083.462 nm) [45]. Off-resonant excitation of the C_5 transition can be induced by the C_3 frequency, which is 1.781 GHz below the C_5 frequency [45]. However, the C_2 and C_4 act as repumpers to repopulate the $F = 3/2$ metastable state [46]. The hyperfine energy intervals in $2\,^3P$ of ^{3}He are provided in [45] and the interval in $2\,^3S_1$ is given in Ref. [47].

is a sufficient starting point for evaporation to quantum degeneracy [21].

Efficient laser cooling is possible in both isotopes as these cooling transitions are *closed*, with a high probably of returning the atom to the initial state after a cycle of photon absorption and decay. In each case a photon absorption initially populates the $2\,^3P_2$ state which predominately decays to the metastable state as a decay to the ground state is forbidden [49]. In the hyperfine structure of ^{3}He* ($I = 1/2$), the excited $F = 5/2$ state can only decay to the $F = 3/2$ metastable state following the selection rule $\Delta F = \pm 1$. In the presence of a magnetic field the (initial) total angular momentum projection may also be maintained after a laser cooling absorption-emission cycle. Here σ^+-polarized cooling light is used to drive the $m_J = 1 \rightarrow m_J = 2$ transition in ^{4}He* ($m_F = 3/2 \rightarrow m_F = 5/2$ transition in ^{3}He*) which can only decay to the original state given the $\Delta M_{F,J} = \pm 1$ selection rule.

While the C_3 cooling transition in ^{3}He* itself is closed, the small energy differences between the excited hyperfine states [45] comparable to their natural linewidths ($\Gamma \approx 1.6$ MHz [50]) means that laser cooling at this frequency will drive other excitations. Specifically there will be a weak off-resonant excitation from the metastable state to the $2\,^3P_2$ ($F' = 3/2$) state (C_5 transition), from which the atom decays to the $2\,^3S_1$ $F = 1/2$ state, resulting in a depletion of the $F = 3/2$ metastable state. However, this depletion is countered by the stronger off-resonant driving of transitions which drive population out of the $F = 1/2$ state. In particular as the detunings of the C_3 laser with respect to the C_2 and C_4 transitions are -249Γ and 169Γ respectively ($\approx 1100\Gamma$ for C_5), the $F = 3/2$ metastable state is quickly repopulated by decay from the $2\,^3P_2$ ($F' = 1/2$) or $2\,^3P_1$ ($F' = 3/2$) states [46]. Therefore, this state leakage is strongly suppressed and an extra laser frequency is not required to excite atoms out of the "dark" ground state for any stage of our experiment. This result was originally confirmed experimentally in Ref. [21].

The detuning between the D_2 and C_3 transitions used to cool each isotope is sufficiently large (33.574 GHz [45]) that there is negligible off-resonant excitation of one isotope's cooling laser from the others' cooling laser.

D. Evaporative and sympathetic cooling

For our system laser cooling alone is not enough to reach quantum degenerate temperatures. We have previously successfully achieved degeneracy in ^{4}He*, reaching BEC, by applying radio-frequency (rf) induced forced evaporation (on the $2\,^3S_1$ $m_J = +1 \rightarrow m_J = 0$ transition) in a magnetic trap [33]. However, this procedure cannot be directly applied to fermionic ^{3}He*. Only the s-wave component of scattering interactions has a nonzero contribution to the scattering amplitude in the low-energy limit. Furthermore, due to the Pauli exclusion principle the s-wave scattering length of fermions is zero, and thus a Fermi gas will be unable to rethermalize with itself via elastic collisions [22]. However, as the fermions are in thermal contact with the bosons and the interspecies scattering length is relatively large [$a_{34} = 29(4)$ nm [51], for sufficiently slow evaporation the fermions will thus remain in thermal equilibrium with bosons as they are cooled. Given that the expected interspecies scattering length is significantly higher than the ^{4}He* intraspecies scattering length [$a_{44} = 7.512(5)$ nm [36]] we were able to use the same evaporation cycle that is used for a pure sample of ^{4}He* (approximately 16 s in length). The change in temperature of the mixture due to the forced evaporation process depends on the efficiency of the evaporation ramp (parametrized by η), the sum of the heat capacities, and the rate of change in energy of the Bose gas with respect to particle number [52]. As the behavior of the thermodynamic properties of the gases changes between the classical and degenerate regimes, especially for a Bose gas, the exact behavior is fairly complex. However, if the heat capacity of the Fermi gas is negligible compared to the heat capacity of the Bose gas for all temperatures greater than T_C, then the final reduced temperature of the Fermi gas T/T_F is only dependent on the ratio N_b/N_f, where N_b and N_f are the number of bosons and fermions in the mixture after evaporation [53]. This implies that having a larger initial number of fermions is equivalent to evaporating closer to the trap bottom (the detuning for zero momentum), in terms of the reduced Fermi temperature (T/T_F) reached. Furthermore, as T_F and T_C are related by Eq. (3) and the mixture is in thermal equilibrium, the reduced temperature of the Bose gas will also only depend on the ratio N_b/N_f. This also implies that for a given evaporation efficiency and initial phase-space density there is an optimal Fermi reduced temperature that can be reached (i.e., when all the coolant, ^{4}He* gas, has been used up).

We expect a negligible amount ^{3}He* to be removed during the evaporation process, even in the thermal regime where the fermionic scattering lengths are nonzero. The energy due to the external magnetic field for a given substate is $E_{m_{F/J}} = g m_{F/J} \mu_B B$, where μ_B is the Bohr magneton, B is the field strength, and g is the gyromagnetic ratio. If we consider the relevant transition for the magnetically trapped substates of each species ($m_J = +1 \rightarrow m_J = 0$ for ^{4}He* and $m_F = +3/2 \rightarrow m_F = +1/2$ for ^{3}He*) and their gyromagnetic ratios ($g = 2$ and $4/3$ respectively) we can see that the resonant frequency for a given magnetic field is $3/2$ times larger for ^{4}He* than it is for ^{3}He*. For our trap minima of $B = 0.3$ G this corresponds to a detuning of ≈ 0.3 MHz. Thus, if ^{3}He* is in thermal equilibrium with ^{4}He* then ^{4}He* will be preferentially evaporated, assuming we start our forced evaporation sweep above the ^{4}He* trap bottom. For further detail on this mechanism see Ref. [21], where we note that preferential evaporation of ^{3}He* was also observed. For a magnetic trap, as used here, this effect is further exacerbated by the ^{3}He* atoms experiencing a $\sqrt{\frac{4}{3}}$ times higher trapping frequency due to their smaller mass, which means that on average they will sit closer to the trap center.

We characterize the evaporation cycle by the detuning, or height, of the final frequency applied from the frequency of the transition for an atom at zero temperature. This is equivalent to the detuning for an atom sitting at the minimum of the trapping potential, thus we refer to this parameter as the evaporation height above trap bottom. Note that once all ^{4}He* atoms have been evaporated, if we continue to lower the evaporator height then ^{3}He* atoms will be removed.

III. APPARATUS

In this section we will cover the technical aspects of our experimental apparatus, focusing on the modification required to incorporate ^{3}He* into the cooling process, specifically the laser and vacuum system.

A. Source of metastable atoms

Before using laser cooling and trapping techniques, we need to first produce metastable helium. However, optically producing He* by exciting helium from the ground state to the $2\,^3S_1$ is impractical, as it would require far ultraviolet light, which is not conveniently accessible, and furthermore the scattering cross section of the transition is extremely small [54]. Therefore, we use high-energy electron collisions in a liquid nitrogen cooled dc discharge plasma to excite both species to the $2\,^3S_1$ state. This plasma is focused by an insulating nozzle through the gas flows before undergoing a supersonic expansion [55]. Atoms with a low transverse velocity are then selected to enter the next stage with a simple mechanical aperture.

B. Atom-optics elements

The atom beam comprising both ^{4}He* and ^{3}He* is initially collimated by cooling in the transverse direction with a two-dimensional optical molasses and then slowed via a Zeeman slower, in which a red-detuned laser light combined with a magnetic field acts to continuously slow the beam. The slowed He* atoms are then captured in a magneto-optic trap (MOT) variant which produces a focused cold beam of He*, which is used to load a second MOT [56]. After transferring the atoms from the MOT to a magnetic trap, 1D Doppler cooling is employed to further cool the atoms [33].

C. Magnetic trap

We perform our 1D Doppler cooling and rf evaporation of the two species in a biplanar quadrupole Ioffe magnetic trap [33], which can be treated as a harmonic potential with cylindrical symmetry. For the data presented in this paper we have used trapping frequencies for ^{4}He* of $\{\omega_x, \omega_y, \omega_z\}/2\pi \approx \{60(2), 600.5(1), 605.7(7)\}$ Hz, with gravity aligned along the z axis. The trapping frequencies were measured using a pulsed atom laser technique described in Ref. [57].

D. Detection

We measure the far-field time-of-flight profiles for both species using a microchannel plate (MCP) and delay line detector [25] system, which due to the high internal energy of both species' metastable state allows us to detect the positions of single atom impacts after they are released from the trap. The MCP is located 858.7 mm below the trap, which corresponds to a fall time of $t_0 = 0.4187$ s, for a particle with zero initial momentum.

As both clouds' momenta distributions are initially centered on zero they will overlap on the detector if they are only influenced by gravity. To separate the clouds we apply a linear magnetic-field gradient to both species, produced by a set of coils surrounding our BEC chamber. While the two isotopes have the same magnetic moment, and hence experience the same force from the external field, they will be accelerated by different amounts due to their differing masses. This pulse alters our time-of-flight profiles and must be accounted for in order to obtain accurate measurements of the mixtures' properties (see Sec. II B).

To avoid detector saturation [25] we employ a pulsed atom laser technique for ^{4}He* [57], which out couples only small portions ($\approx$2%) of the cloud, with each pulse being well below the saturation limit and thus giving an accurate measure of the ^{4}He* atom number. In order to determine the atom number of the ^{3}He* cloud we employ absorption imaging. The linear polarization of our probe beam will pump the imaged atoms into a steady state after some time (approximately 50 μs for our experiment). Using the relevant Clebsch-Gordan coefficients we can solve for the steady-state distribution and find a 25/14 increase in our saturation intensity for ^{3}He*. Hence, we can find the number of ^{3}He* atoms in our mixture via the relation $N_f = \frac{1}{\sigma_a}\iint dxdy\, D(x, y)$, where the optical density D is defined as $I_{\text{out}} = I_{\text{in}}e^{-D}$ and the absorption cross section σ_a is the absorption cross section [58].

E. Recirculation system

The plasma discharge source used to create He* is relatively inefficient with only a small fraction (10^{-8}) of the helium atoms input into the source being converted into He* and making it into the first stage of the system (transverse cooling). The remaining gas is pumped away with a turbo molecular pump and previously had been discharged to atmosphere via the exhaust of a backing pump.

While this approach is reasonable with ^{4}He, which is relatively inexpensive, the cost of ^{3}He means that this approach would quickly become prohibitive given the relatively high flow rate [0.7(1) NTP L/h] required by the source. We have therefore implemented a system which can recycle this helium gas while maintaining the high purity required for an efficient metastable producible.

The plasma source of He* is quite sensitive to contaminants owing to both gas interactions and mechanical effects. First in a gas of helium and metastable helium the presence of impurities acts to destroy the metastable component through a process known as penning ionization. This process is highly favored for almost all impurity atoms (except for neon) given the large helium metastable state energy compared to the impurities' ionization energy. Furthermore, contaminants can mechanically degrade the source; organics such as oil are decomposed by the source into carbon soot, while impurities such as oxygen accelerate the erosion of the copper and tungsten materials of the source. In the previous system contaminants were avoided by using high-purity helium gas, however in the recycling system oil from the vacuum pumps and the inevitable leakage of air into the system will accumulate and must be dealt with.

To recycle the gas requires compressing the gas that is captured by the three relevant turbo vacuum pumps (see Fig. 2), to the pressure needed to run the discharge source (between 10 and 0.5 kPa), and then feeding it back into the source. To reduce the source of oil as much as possible we replaced the rotary-vane backing pump for the source turbo, which uses oil

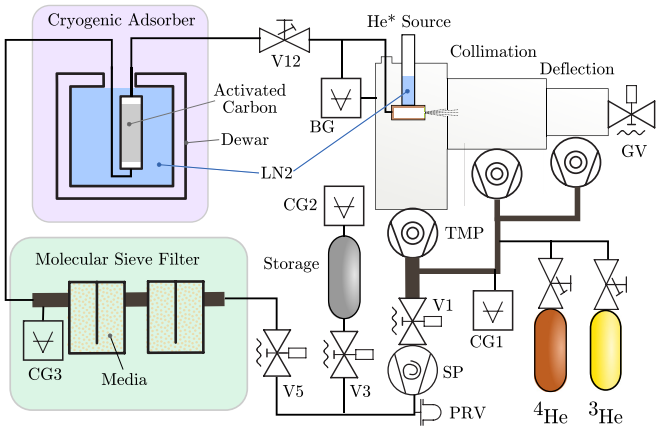

FIG. 2. Simplified schematic of the recycling system. TMP, turbomolecular pump; SP, scroll pump; PRV, pressure release valve; BG, baratron gauge; LN2, liquid nitrogen; GV, gate valve; V, valve; CV, convectron.

as a sealing and lubricating agent, with a "dry" (oil-free) scroll pump. This does not eliminate oil from the system entirely as all three of the turbomolecular pumps use oil lubrication of the rear bearing. To manage this contamination two filter stages are used. First, on the backing line of the turbomolecular pumps we use micromaze traps comprising a number of highly porous ceramic plates that trap oil vapor. This serves to reduce the contamination of the scroll pump which compresses the gas to the source pressure. After compression the gas then passes through two molecular sieve filters filled with SSZ-13 zeolite media. This second stage further reduces oil and presents a large surface area which also serves to adsorb water vapor. The molecular sieves can be partially regenerated by removing the circulating gas and heating them to approximately 120 °C.

As the recycling system is closed, any small air leaks will compound over time. To remove this air the final filtration stage uses a liquid nitrogen cooled activated carbon adsorber. At low temperatures gas molecules make a weak van der Waals bond to the carbon surface through a process known as adsorption which is maximized by using activated carbon with a large surface area. Operation of the adsorber at liquid nitrogen temperatures is able to remove all atmospheric gases (oxygen, nitrogen, water) while preventing adsorption of helium. To regenerate the adsorber the liquid nitrogen is removed from the surrounding dewar and the unit heated to ≈120 °C. During regeneration of the adsorber and the molecular sieves the helium gas is stored in a separate storage tank.

A key parameter for engineering this system is the amount of ^{3}He needed to fill the system. This is set by the volume (tubing and filters) which is pressurized to the pressure required to start the source plasma. This pressure is decreased (compared to our previous design) to a few kPa by using a flyback based high voltage ignition system from a residential barbecue. The total volume at the source pressure is kept to 5 L, while the total gas needed to operate the system is then 0.1 L STP, which in a 50:50 ratio of ^{3}He to ^{4}He represents a few hundred AUD of ^{3}He.

The recycling system only captures gas before the Zeeman slower. However, the loss of helium which goes beyond this point from both the helium background gas pressure (1×10^{-2} L STP/year) and metastable flux (2×10^{-4} L STP/year) is acceptably small.

As a test of operation, ^{4}He has been successfully recirculated for months at a time without problem. A residual gas analyzer fixed to the collimator stage was used to monitor the gas composition of the source, with no detectable impurities above the background levels in the chamber.

F. Laser lock

A laser with a stable frequency is important for cooling and trapping an atomic gas. In our setup an external-cavity laser (ECL) system is used for ^{4}He* [59], featuring a diffraction grating that selects the coarse laser frequency. The grating is installed on a piezoelectric chip (PZT) that changes the cavity length and finely modulates the frequency. This ECL is locked to the D_2 transition in ^{4}He* using saturated absorption spectroscopy (SAS) [59]. For He*, the need to have an excited-state population means that SAS requires an rf discharge driven plasma inside the vapor cell as an atomic reference. Due to problems caused by the plasma etching, the cell needs to be refilled regularly. However, because of the high cost of ^{3}He gas we have utilized an alternative setup, based on a frequency comb and a phase-locked loop, which locks the ^{3}He* laser relative to the ^{4}He* laser by stabilizing the beat frequency between the two lasers.

As discussed in Sec. II C, the ^{3}He* laser is locked to the C_3 transition [$2\,^3S_1(F = 3/2) \rightarrow 2\,^3P_2(F' = 5/2)$], which is 33.574 GHz red-detuned from the ^{4}He* D_2 transition ($2\,^3S_1 \rightarrow 2\,^3P_2$). This detuning is too large for conventional electronics to easily process. To circumvent this we used a high-frequency optical phase modulator (ixblue NIR-MPX-LN-10) to create a small span frequency comb, with the ^{4}He* laser as the carrier frequency (f_c) and tooth spacing f_m set by the modulation frequency [60,61]. Specifically the Nth-order tooth (or sideband) has the frequency $f_c \pm N f_m$. For our experiment $f_m \approx$ 10 GHz and is set by a microwave synthesizer (Windfreak SynthHD v2).

The ^{3}He* laser is then mixed with light from the frequency comb on a photodiode, generating a series of beat frequencies equal to the absolute value of the offset between the ^{3}He* laser and the sidebands. The lowest of these beat notes [$f_{b1} = |f_{^3\mathrm{He}} - (f_c + N f_m)|$] is for the third-order lower sideband $N = -3$ in our system, and is at most 5 GHz. The beat note can be reduced to arbitrarily small values via tuning f_m, for our experiment $f_{b1} \approx 1$ GHz. The value of f_{b1} is actively stabilized by a feedback loop that compares it with a reference frequency using a fractional-N phase frequency detector (Linear Technology LTC6947). The LTC6947 board outputs a signal proportional to the phase and frequency difference between f_{b1} and the target frequency. The error signal is then used to stabilize f_{b1} through both a fast proportional-only path to the ^{3}He* laser diode current and a slower proportional-integral (PI) path which controls the PZT of the ^{3}He* laser. As $f_c + N f_m$ is fixed stabilizing f_{b1} is equivalent to stabilizing $f_{^3\mathrm{He}}$. In this system we find the frequency difference between the ^{3}He* C_3 transition and $f_{^3\mathrm{He}}$ (Δ_{C3}) using the previously measured frequency difference of D_2 and C_3, $\Delta_{C3} = f_{^3\mathrm{He}} - f_{^4\mathrm{He}} + 33\,574$ MHz [45]. This procedure is illustrated

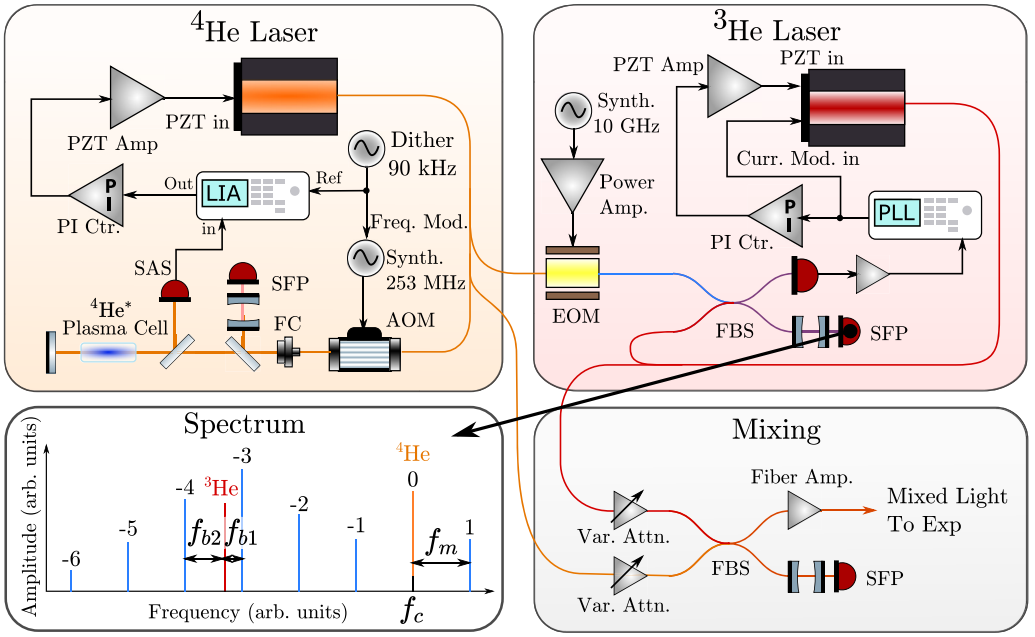

FIG. 3. Laser system. Sidebands of the ^{4}He* laser are generated by an EOM, driven by a MW frequency synthesizer. The ^{4}He* light, together with its sidebands, is mixed with the ^{3}He* laser on a photodiode, synthesizing a series of beat signals. One of the beat notes is chosen as the input to the PLL, whose output controls the current modulation of the laser and is also sent to a PI controller. After being integrated by the PI controller, the output is fed back to the PZT of the ^{3}He* laser to actively lock its frequency to the expected value. AOM, acousto-optic modulator; EOM, electro-optic modulator; Var. Attn., electronic variable optical attenuator; PZT, piezoelectric actuator; Curr. Mod, current modulation; Freq. Mod., frequency modulation; Synth. 10 GHz, Windfreak MW synthesizer; PI Ctr., proportional integral controller; SAS, saturation absorption spectroscopy; FBS, fiber beamsplitter; SFP, scanning Fabry-Pérot interferometer. In the spectrum, with a phase modulation of 4.4 rad, the third sideband amplitude is 0.22. The parameters f_{b1} and f_{b2} are the lowest-frequency beat notes produced when the ^{3}He laser is mixed with the frequency comb generated with the EOM.

in Fig. 3, which also shows an indicative spectrum of the frequency comb.

The linewidth of the beat note is one of the primary indicators of the performance of the laser lock. To evaluate the linewidth, a Gaussian is fitted to the central region that spans ≈1 MHz of its spectrum and a Lorentzian is fitted to the tails [62,63]. Figure 4 shows the linewidths measured for a series of sweep times of the spectral analyzer. The linewidth is deduced to be on the order of 100 kHz, which is larger than the linewidth of the ^{4}He* laser (≈33 kHz [59]), as is expected, but much smaller than the natural linewidth of the relevant transitions ($\Gamma \approx 1.6$ MHz). The Allan deviation $\sigma(\tau)$ (shown in Fig. 4) indicates that the laser could readily be used in spectroscopic measurements, with a measurement uncertainty of ≈5 kHz only requiring 10 s of integration time. This system could in principle be used to stabilize even larger frequency offsets by increasing the modulation drive power and using higher modulation orders. It could also lock multiple lasers at the same time as the maximum beat note frequency (5 GHz) can be readily captured on a photodiode.

Incorporating ^{3}He* light into the existing ^{4}He* BEC experimental apparatus [33] required overlapping the ^{3}He* laser with the ^{4}He* laser for every atom-optic element of the apparatus. Previously, cooling light for ^{4}He* was produced by amplifying light from the master laser with a fiber amplifier (Nufern, NUA-1064-PB-0005-A2). To cool both ^{3}He* and ^{4}He* we seed this fiber amplifier with a mixture of C_3 and D_2

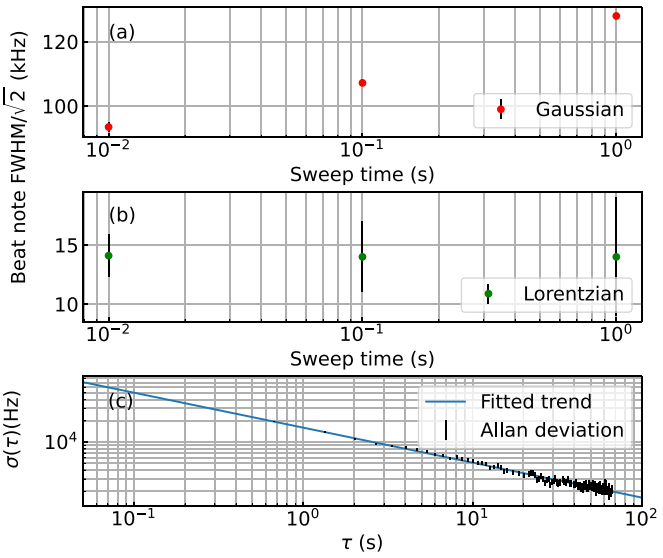

FIG. 4. (a), (b) FWHM/$\sqrt{2}$ of the Gaussian and Lorentzian of the locked beat note for different sweep times respectively. As the sweep time increases, the beat note linewidth given by the Gaussian shows an increasing trend while the linewidth estimated by the Lorentzian remains stable. The beat note is estimated to have a linewidth of ≈100 kHz. (c) Allan deviation $\sigma(\tau)$ of the beat note frequency. It decreases over time as the noise of the signal measured at different times cancels out. The fitted relationship between σ and integration time τ is $\sigma(\tau) = 16\,037\sqrt{\text{Hz}}\,\tau^{-1/2}$.

cooling light. The output of the amplifier then contains both frequencies of light, which is overlapped in the atom-optic elements previously arranged for the ^{4}He* laser. This avoids duplicating many of the optical components of ^{3}He*. The ratio of the frequency components at the output is then dynamically controlled using electronically variable attenuators on the inputs. Furthermore, we have measured the ratio of output powers for the two wavelengths using a scanning Fabry-Pérot cavity and have found it to be very stable over time. We have found that the spatial overlap for the frequency components along the optical path is robust even with the incision of acousto-optic modulators (AOMs). In this approach, the independent control of the detuning of ^{3}He and ^{4}He cooling light for each atom-optic stage via the AOM is compromised for the simplicity and convenience of overlapping the two lasers using the fiber amplifier. In contrast, in the previous experimental realization [21] a second cooling laser was added to cool ^{3}He*, which meant they also implemented a new AOM for each optical cooling section and then manually overlapped the optical paths with the ^{4}He* beams, which allowed for full independent control of the cooling stages for each isotope. As we only need to sympathetically cool a limited amount of ^{3}He* [52], this compromise only leads to a minimal decrease from the optimal conditions that would be possible with independent optics for each laser. This can also be clearly seen by comparing the results of our apparatus with that of Ref. [21], as will be discussed in Sec. IV B.

IV. RESULTS

In this section we will discuss the level of degeneracy achieved in our Bose-Fermi mixture, along with how our main two control parameters, detuning of the ^{3}He* laser and final stage rf evaporator height, affect the most relevant experimental parameters, reduced temperature and atom number of the respective gases.

A. Time-of-flight profiles

We find the temperature of the final mixture from the high momentum tails of the time-of-flight profile of the ^{4}He* atoms (see Fig. 5). This is due to a number of factors; however, it is primarily because it is difficult to accurately fit the temperature and fugacity of Fermi-Dirac distribution independently as there is strong cross correlation between their values, significantly stronger than in the Bose-Einstein distribution (see Ref. [41] for further details). However, we still fit the Fermi-Dirac distribution as a verification of the order of magnitude of the temperature measurement of the ^{4}He* cloud.

This approach of thermometry using only the ^{4}He* cloud assumes that both gases are in thermal equilibrium at the time of release from the trap. Due to the high scattering length between the species $a_{34} = 29(4)$ nm [51] we expect them to thermalize relatively quickly. However, due to the difficulty of extracting the temperature from the Fermi distribution accurately we cannot confirm this directly. In the data presented here we hold the clouds for 400 ms after the end of evaporation.

B. Dependence on laser detuning and evaporator height

As the same relative detuning along the shared optical path is employed for both ^{3}He* and ^{4}He* for all cooling we are effectively only able to change the initial amount of ^{3}He* in our final magnetic trap via three methods: The ratio of the amount of ^{3}He and ^{4}He gas in the metastable source; the ratio of power between ^{3}He and ^{4}He light (controlled by changing the ratio of power in the seed light); and the detuning of the ^{3}He seed light from its cooling transition, which can be controlled independently of the detuning of the ^{4}He seed light. For this paper we only focus on the behavior of ^{3}He detuning as it is the only parameter of the three that changes the initial amount of ^{3}He* atoms while leaving the initial amount and temperature of ^{4}He* atoms completely unchanged. All relative detuning and alignment of optomechanical components are optimized for ^{4}He* flux. As will be shown this is reasonable, as even with suboptimal conditions for ^{3}He* we can still load more ^{3}He* into the magnetic trap than we can effectively cool [52]. In Fig. 6 we show how the atom numbers, temperature, and reduced temperatures vary with ^{3}He detuning ($f_{^3\mathrm{He}} - f_{^4\mathrm{He}}$) for a fixed evaporator height of 15 kHz. There is a region around zero detuning ($\Delta_{C3} = 0$) where all ^{4}He* atoms are evaporated. We do not present a temperature measurement in this region due to the unreliability of the temperature measurement from the fermionic cloud. In this data set we have a minimum boson reduced temperature of $T/T_C = 0.25(1)$. Note that our system is capable of achieving significantly lower reduced temperatures of the boson cloud, however here we deliberately keep a significant portion of the ^{4}He* cloud thermal in order to more easily measure the temperature.

In Fig. 7 we investigate the effect of evaporator height on the mixture's reduced temperatures and atom number with a fixed ^{3}He* detuning of $\Delta_{C3} = 0.75$ MHz. As expected, the mixtures, temperature, and ^{4}He* atom number decrease with evaporator height, while the ^{3}He* atom number remains roughly constant until almost all ^{4}He* atoms have been evaporated. The Fermi reduced temperature hence decreases with evaporator height, while the Bose reduced temperature increases when there is a nonzero number of ^{3}He* atoms.

As discussed in Sec. II D, the behavior of the reduced temperatures seen in Figs. 6 and 7 can be understood purely by how each variable (detuning of the ^{3}He* laser and final evaporator height) affects the ratio N_b/N_f. In Fig. 8 we show how the Bose and Fermi reduced temperatures T/T_C and T/T_F vary with the atom number ratio N_b/N_f. We find that the Fermi reduced temperature follows the expected relation derived from comparing heat capacities of the coolant (^{4}He*) to the atom being sympathetically cooled (^{3}He*), and modeling the forced evaporation as a temperature dependent energy cutoff [52,53]. For our system the Bose and Fermi critical temperatures are related purely via the atom number ratio [Eq. (3)]. Thus, we can convert the relation between the Fermi reduced temperature and the atom number ratio to a relation for the Bose reduced temperature.

Note that this relation holds regardless of the method by which these parameters are changed. This implies an optimal Fermi reduced temperature for our current experimental conditions of $T/T_F = 0.18(3)$, in the limit of complete evaporation of ^{4}He*. This compares well to the minimum

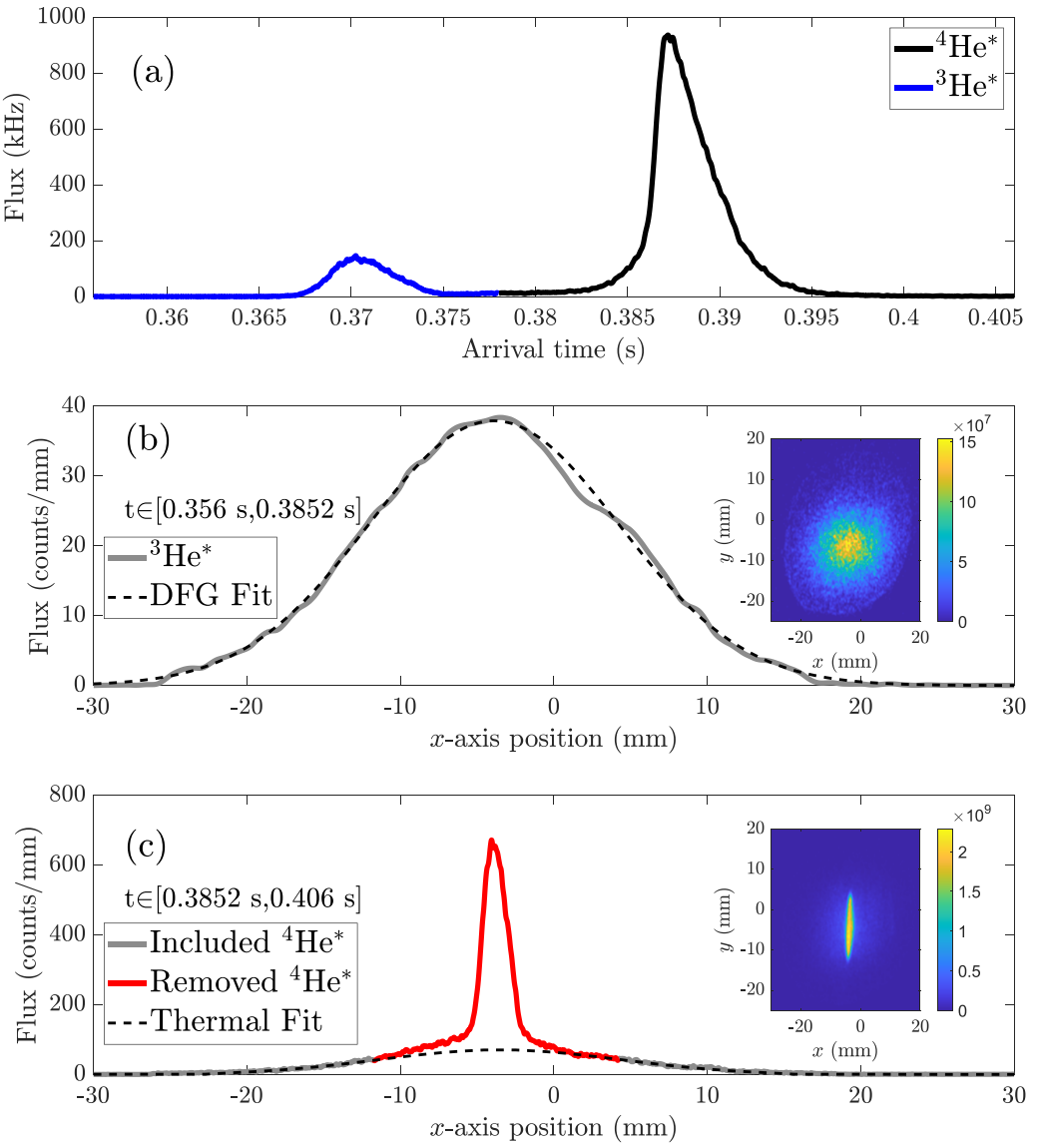

FIG. 5. Time-of-flight profiles for ^{3}He* and ^{4}He* for a final evaporation height of 15 kHz and detuning$\Delta_{C3} = 1.0$ MHz. (a) We show the flux as a function of arrival time after trap switch off. The two species are separated in time by using a magnetic-field gradient. The ^{3}He* cloud lands on the detector first and is highlighted in blue, while the center of the ^{4}He* cloud arrives 10 ms later. Some saturation of the BEC is present in the ^{4}He* profile, however this is not an issue as we do not derive any information from this section of the profile. (b) Average x-axis flux of the ^{3}He* cloud fitted with a Fermi-Dirac distribution with $T = 174(10)$ nK, and $\xi = 3.8(2)$ (black dashed line). Inset: Density distribution over the x-y plane, demonstrating the isotropy of the cloud. (c) Average x-axis flux of the ^{4}He* cloud. We fit a thermal distribution (black dashed line) with $T = 215(18)$ nK to the wings of the distribution, colored in gray, removing the central area which is either overlapped with the condensate or affected by its mean field, colored in red. We fit along the x axis as this is has the smallest BEC momentum width. This corresponds to a reduced temperature of $T/T_F = 0.40(4)$ for the fermions and $T/T_C = 0.29(5)$ for bosons. Inset: Density distribution over the x-y plane, demonstrating the anisotropy of the BEC.

experimentally observed reduced temperature of $T/T_F = 0.14(1)$, achieved for an evaporator height of 15 kHz and ^{3}He* laser detuning of $\Delta_{C3} = -1.6$ MHz. We note that this value is well into the quantum degenerate regime. We also wish to highlight that this minimum reduced temperature is considerably lower than that reported by Ref. [21] of $T/T_F = 0.45$ where there was independent control of the individual atom optic elements, albeit we finish with a lower total atom number of ^{3}He*.

V. CONCLUSION

In this paper, we have successfully produced a degenerate Fermi gas of ^{3}He*, with a minimum reduced temperature of $T/T_F = 0.14(1)$, via sympathetic cooling with ^{4}He* that is undergoing forced evaporation. The limiting reduced temperature could be improved further by using dynamic control of the relative intensity of the two frequencies of light, such that it is optimized for each stage of the experiment. This is especially relevant for the 1D Doppler cooling employed

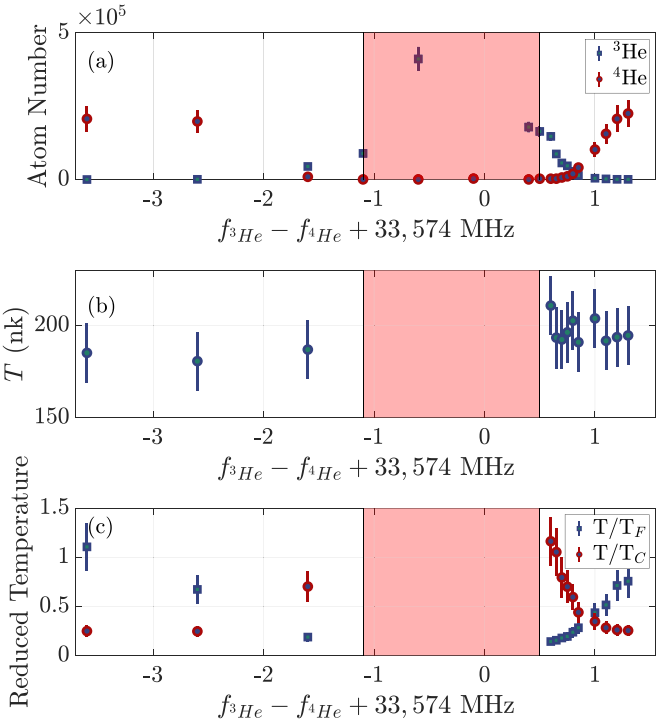

FIG. 6. Atom numbers (a), temperature (b), and reduced temperature (c) of both species of the Bose-Fermi mixture against the detuning of the ^{3}He* laser from the cooling transition (Δ_{C3}) for a fixed evaporator height of 15 kHz. This allows us to effectively load various amounts of ^{3}He* atoms into the trap, while leaving the initial number and temperature of the ^{4}He* atoms unchanged. The region with no ^{4}He* atoms is shaded red. We do not present temperature measurements in this region as our temperature measure from the Fermi cloud is unreliable.

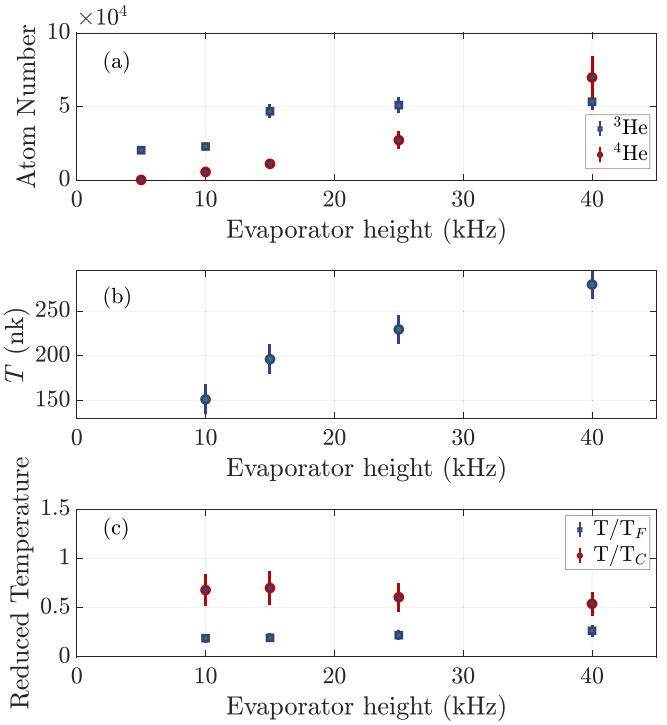

FIG. 7. Atom numbers (a), temperatures (b), and reduced temperature (c) vs the final height of the forced evaporation above the trap bottom, for a fixed ^{3}He* detuning of $\Delta_{C3} = 0.75$ MHz. Note that the ^{3}He* number remains unchanged until almost all the ^{4}He* have been evaporated, as expected. Furthermore, we see that while the temperature of the mixture decreases with evaporator height, the reduced temperatures remain roughly constant, with only a slight reduction in T/T_F.

to initially cool both species, as this stage has a very strong effect on the initial phase-space density of the mixture. The minimum reduced temperature can also be improved simply by increasing the heat capacity of the initial ^{4}He* sample.

The technique presented creates an excellent platform for a range of possible experiments in the areas of many-body physics, quantum atom optics, and Bose-Fermi mixtures. The capability of single-particle detection for ^{3}He* provides the opportunity to measure many-body correlations that display higher-order antibunching, which has so far been unobserved. This behavior is the equivalent Hanbury Brown–Twiss effect for fermions, which has been used to experimentally observe higher-order bunching in bosonic ^{4}He* atoms [64,65], and second-order (two-body) antibunching in fermionic ^{3}He* [2]. Single atom detection also allows access to interesting many-body phenomena, such as creating an *s*-wave scattering halo [66] between a highly degenerate BEC and DFG, which will have a nontrivial range of Bose bunching and Fermi antibunching across the different correlation functions.

Furthermore, this *s*-wave scattering can be used to obtain a momentum entangled state of ^{3}He* and ^{4}He*. Such a state could be used to test the validity of the weak equivalence principle for a nonclassical state [31]. While the weak equivalence principle has been extensively tested in the classical regime, its validity for quantum entities is still an open question.

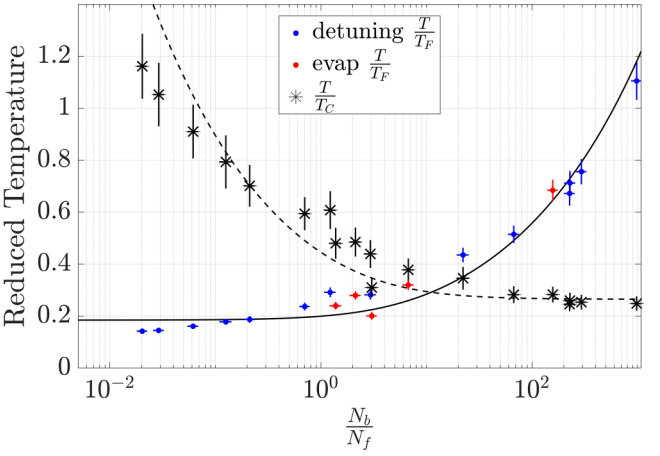

FIG. 8. The reduced temperatures T/T_F and T/T_C plotted against the ratio of the number of bosons to fermions after the evaporation cycle. We see that T/T_F and N_b/N_f are equivalently related (solid line) for small changes to either the initial number of fermions (blue points) or evaporator height (red points) [53]. Using the relation $T/T_C = 2.23(\frac{N_b}{N_f})^{-1/3} T/T_F$ we plot the T/T_C dependence on N_b/N_f (dashed line). The minimum of the average reduced temperature of both species is achieved for $T/T_C = 0.31(4)$ and $T/T_F = 0.20(3)$ with $N_b/N_f = 3.0(4)$.

Another area of possible future work is investigating many-body physics using DFGs and Bose-Fermi mixtures of He^* in lower-dimensional dipole traps or optical lattices. Such experimental work using $^4He^*$ has leveraged the single atom resolution to produce a variety of interesting results [67–70]. A lower-dimensional trap or optical lattice with $^3He^*$ has yet to be achieved; however, this would be an interesting area of future research.

This system opens up a number of interesting potential experiments in the area of scattering physics, for example the measurement of the $^3He^*$ - $^4He^*$ s-wave scattering length a_{34} experimentally for the first time, and investigating the possibility of Fermi-Fermi interactions between identical fermions mediated by the Bosonic atoms. In the latter while spin polarized ultracold fermions cannot directly interact with each other, they can interact with bosons, which can serve to create an effective interaction between the fermions. Finally, this system could also be used to continue our spectroscopic investigation of the atomic structure of helium, allowing us to observe thus far unseen quantum electrodynamic effects [3,29,30].

ACKNOWLEDGMENTS

This work was supported through Australian Research Council Discovery Project Grant No. DP190103021. K.F.T. and B.M.H. were supported by Australian Government Research Training Program scholarships. We would also like to thank Prof. Robert Scholten for his helpful advice and guidance, particularly regarding the laser system.

[1] M. H. Anderson, J. R. Ensher, M. R. Matthews, C. E. Wieman, and E. A. Cornell, Observation of Bose-Einstein condensation in a dilute atomic vapor, Science **269**, 198 (1995).

[2] T. Jeltes, J. M. McNamara, W. Hogervorst, W. Vassen, V. Krachmalnicoff, M. Schellekens, A. Perrin, H. Chang, D. Boiron, A. Aspect, and C. I. Westbrook, Comparison of the Hanbury Brown-Twiss effect for bosons and fermions, Nature (London) **445**, 402 (2007).

[3] B. M. Henson, J. A. Ross, K. F. Thomas, C. N. Kuhn, D. K. Shin, S. S. Hodgman, Y.-H. Zhang, L.-Y. Tang, G. W. F. Drake, A. T. Bondy, A. G. Truscott, and K. G. H. Baldwin, Measurement of a helium tune-out frequency: An independent test of quantum electrodynamics, Science **376**, 199 (2022).

[4] T. Byrnes, K. Wen, and Y. Yamamoto, Macroscopic quantum computation using Bose-Einstein condensates, Phys. Rev. A **85**, 040306(R) (2012).

[5] T. Byrnes, D. Rosseau, M. Khosla, A. Pyrkov, A. Thomasen, T. Mukai, S. Koyama, A. Abdelrahman, and E. Ilo-Okeke, Macroscopic quantum information processing using spin coherent states, Opt. Commun. **337**, 102 (2015).

[6] P. A. Murthy, M. Neidig, R. Klemt, L. Bayha, I. Boettcher, T. Enss, M. Holten, G. Zürn, P. M. Preiss, and S. Jochim, High-temperature pairing in a strongly interacting two-dimensional Fermi gas, Science **359**, 452 (2018).

[7] M. W. Zwierlein, J. R. Abo-Shaeer, A. Schirotzek, C. H. Schunck, and W. Ketterle, Vortices and superfluidity in a strongly interacting Fermi gas, Nature (London) **435**, 1047 (2005).

[8] J. K. Chin, D. Miller, Y. Liu, C. Stan, W. Setiawan, C. Sanner, K. Xu, and W. Ketterle, Evidence for superfluidity of ultracold fermions in an optical lattice, Nature (London) **443**, 961 (2006).

[9] I. Bloch, J. Dalibard, and W. Zwerger, Many-body physics with ultracold gases, Rev. Mod. Phys. **80**, 885 (2008).

[10] S. Giorgini, L. P. Pitaevskii, and S. Stringari, Theory of ultracold atomic Fermi gases, Rev. Mod. Phys. **80**, 1215 (2008).

[11] F. M. Marchetti, C. J. M. Mathy, D. A. Huse, and M. M. Parish, Phase separation and collapse in Bose-Fermi mixtures with a Feshbach resonance, Phys. Rev. B **78**, 134517 (2008).

[12] S. G. Bhongale and H. Pu, Phase separation in a mixture of a Bose-Einstein condensate and a two-component Fermi gas as a probe of Fermi superfluidity, Phys. Rev. A **78**, 061606(R) (2008).

[13] J. Linder and A. Sudbø, Probing phase separation in Bose-Fermi mixtures by the critical superfluid velocity, Phys. Rev. A **81**, 013622 (2010).

[14] C.-H. Wu, I. Santiago, J. W. Park, P. Ahmadi, and M. W. Zwierlein, Strongly interacting isotopic Bose-Fermi mixture immersed in a Fermi sea, Phys. Rev. A **84**, 011601(R) (2011).

[15] I. Fritsche, C. Baroni, E. Dobler, E. Kirilov, B. Huang, R. Grimm, G. M. Bruun, and P. Massignan, Stability and breakdown of Fermi polarons in a strongly interacting Fermi-Bose mixture, Phys. Rev. A **103**, 053314 (2021).

[16] B. DeMarco and D. S. Jin, Onset of Fermi degeneracy in a trapped atomic gas, Science **285**, 1703 (1999).

[17] A. G. Truscott, K. E. Strecker, W. I. McAlexander, G. B. Partridge, and R. G. Hulet, Observation of Fermi pressure in a gas of trapped atoms, Science **291**, 2570 (2001).

[18] R. Onofrio, Cooling and thermometry of atomic Fermi gases, Phys. Usp. **59**, 1129 (2016).

[19] G. Roati, F. Riboli, G. Modugno, and M. Inguscio, Fermi-Bose Quantum Degenerate ^{40}K - ^{87}Rb Mixture with Attractive Interaction, Phys. Rev. Lett. **89**, 150403 (2002).

[20] K. Günter, T. Stöferle, H. Moritz, M. Köhl, and T. Esslinger, Bose-Fermi Mixtures in a Three-Dimensional Optical Lattice, Phys. Rev. Lett. **96**, 180402 (2006).

[21] J. M. McNamara, T. Jeltes, A. S. Tychkov, W. Hogervorst, and W. Vassen, Degenerate Bose-Fermi Mixture of Metastable Atoms, Phys. Rev. Lett. **97**, 080404 (2006).

[22] W. Geist, A. Idrizbegovic, M. Marinescu, T. A. B. Kennedy, and L. You, Evaporative cooling of trapped fermionic atoms, Phys. Rev. A **61**, 013406 (1999).

[23] M. J. Holland, B. DeMarco, and D. S. Jin, Evaporative cooling of a two-component degenerate Fermi gas, Phys. Rev. A **61**, 053610 (2000).

[24] F. Schreck, G. Ferrari, K. L. Corwin, J. Cubizolles, L. Khaykovich, M.-O. Mewes, and C. Salomon, Sympathetic cooling of bosonic and fermionic lithium gases towards quantum degeneracy, Phys. Rev. A **64**, 011402(R) (2001).

[25] A. G. Manning, S. S. Hodgman, R. G. Dall, M. T. Johnsson, and A. G. Truscott, The Hanbury Brown-Twiss effect in a pulsed atom laser, Opt. Express **18**, 18712 (2010).

[26] A. G. Manning, R. I. Khakimov, R. G. Dall, and A. G. Truscott, Wheeler's delayed-choice gedanken experiment with a single atom, Nat. Phys. **11**, 539 (2015).

[27] R. Lopes, A. Imanaliev, A. Aspect, M. Cheneau, D. Boiron, and C. I. Westbrook, Atomic Hong-Ou-Mandel experiment, Nature (London) **520**, 66 (2015).

[28] P. Dussarrat, M. Perrier, A. Imanaliev, R. Lopes, A. Aspect, M. Cheneau, D. Boiron, and C. I. Westbrook, Two-Particle Four-Mode Interferometer for Atoms, Phys. Rev. Lett. **119**, 173202 (2017).

[29] R. van Rooij, J. S. Borbely, J. Simonet, M. D. Hoogerland, K. S. E. Eikema, R. A. Rozendaal, and W. Vassen, Frequency metrology in quantum degenerate helium: Direct measurement of the $2^3S_1 \rightarrow 2^1S_0$ transition, Science **333**, 196 (2011).

[30] R. J. Rengelink, Y. van der Werf, R. P. M. J. W. Notermans, R. Jannin, K. S. E. Eikema, M. D. Hoogerland, and W. Vassen, Precision spectroscopy of helium in a magic wavelength optical dipole trap, Nat. Phys. **14**, 1132 (2018).

[31] R. Geiger and M. Trupke, Proposal for a Quantum Test of the Weak Equivalence Principle with Entangled Atomic Species, Phys. Rev. Lett. **120**, 043602 (2018).

[32] R. P. M. J. W. Notermans, R. J. Rengelink, and W. Vassen, Comparison of Spectral Linewidths for Quantum Degenerate Bosons and Fermions, Phys. Rev. Lett. **117**, 213001 (2016).

[33] R. Dall and A. Truscott, Bose-Einstein condensation of metastable helium in a bi-planar quadrupole Ioffe configuration trap, Opt. Commun. **270**, 255 (2007).

[34] C. J. Pethick and H. Smith, *Bose-Einstein Condensation in Dilute Gases* (Cambridge University, New York, 2008)

[35] Y. Castin and R. Dum, Bose-Einstein Condensates in Time Dependent Traps, Phys. Rev. Lett. **77**, 5315 (1996).

[36] S. Moal, M. Portier, J. Kim, J. Dugué, U. D. Rapol, M. Leduc, and C. Cohen-Tannoudji, Accurate Determination of the Scattering Length of Metastable Helium Atoms Using Dark Resonances between Atoms and Exotic Molecules, Phys. Rev. Lett. **96**, 023203 (2006).

[37] G. Baym and C. J. Pethick, Ground-State Properties of Magnetically Trapped Bose-Condensed Rubidium Gas, Phys. Rev. Lett. **76**, 6 (1996).

[38] D. A. Butts and D. S. Rokhsar, Trapped Fermi gases, Phys. Rev. A **55**, 4346 (1997).

[39] B. L. DeMarco, *Quantum Behavior of an Atomic Fermi Gas* (University of Colorado, Boulder, CO, 2001).

[40] I. Yavin, M. Weel, A. Andreyuk, and A. Kumarakrishnan, A calculation of the time-of-flight distribution of trapped atoms, Am. J. Phys. **70**, 149 (2002).

[41] If we wish to fit a thermal distribution to the wings of our time-of-flight profiles it is relevant to know that for a given reduced temperature and momentum cutoff (i.e., all data with momenta smaller than the cutoff are ignored for purpose of the fitting) the fitted temperature is more strongly dependent on the fugacity for fermions, compared to bosons. There is a small factor which contributes to this specific to our experiment, namely, $v_b < v_f$ for a fixed temperature as $m_b > m_f$, and thus the Bose distribution decays more rapidly. The primary factors are that the Fermi fugacity ξ_f grows significantly faster with respect to reduced temperature τ compared to the Bose fugacity ξ_b. This can be readily seen from the relations $\tau^{-3/2} = \Gamma(5/2)\mathrm{Li}_{\frac{3}{2}}(\xi_b)$ and $\tau^{-3/2} = -\Gamma(5/2)\mathrm{Li}_{\frac{3}{2}}(-\xi_f)$ which are valid for a harmonic trap [42]. Furthermore, Fermi fugacity has a stronger effect on the high momentum wings as it has a broadening effect on the distribution (compared to a purely thermal distribution). Conversely, the Bose distribution narrows with increasing fugacity and thus is less affected in the wings.

[42] B. Cowan, On the chemical potential of ideal Fermi and Bose gases, J. Low Temp. Phys. **197**, 412 (2019).

[43] S. S. Hodgman, R. G. Dall, L. J. Byron, K. G. H. Baldwin, S. J. Buckman, and A. G. Truscott, Metastable Helium: A New Determination of the Longest Atomic Excited-State Lifetime, Phys. Rev. Lett. **103**, 053002 (2009).

[44] P. C. Pastor, G. Giusfredi, P. DeNatale, G. Hagel, C. de Mauro, and M. Inguscio, Absolute Frequency Measurements of the $2\,^3S_1 \rightarrow 2\,^3P_{0,1,2}$ Atomic Helium Transitions around 1083 nm, Phys. Rev. Lett. **92**, 023001 (2004).

[45] J. D. Prestage, C. E. Johnson, E. A. Hinds, and F. M. J. Pichanick, Precise study of hyperfine structure in the $2\,^3$p state of ^{3}He, Phys. Rev. A **32**, 2712 (1985).

[46] R. J. W. Stas, Trapping Fermionic and Bosonic Helium Atoms, Ph.D. thesis, Vrije Universiteit Amsterdam, 2005.

[47] S. D. Rosner and F. M. Pipkin, Hyperfine structure of the 2^3S_1 state of He^3, Phys. Rev. A **1**, 571 (1970).

[48] T. Jeltes, Quantum Statistical Effects in Ultracold Gases of Metastable Helium, Ph.D. thesis, Vrije Universiteit Amsterdam, 2008.

[49] S. S. Hodgman, R. G. Dall, K. G. H. Baldwin, and A. G. Truscott, Complete ground-state transition rates for the helium $2\,^3P$ manifold, Phys. Rev. A **80**, 044501 (2009).

[50] W. Vassen, C. Cohen-Tannoudji, M. Leduc, D. Boiron, C. I. Westbrook, A. Truscott, K. Baldwin, G. Birkl, P. Cancio, and M. Trippenbach, Cold and trapped metastable noble gases, Rev. Mod. Phys. **84**, 175 (2012).

[51] T. M. F. Hirsch, D. G. Cocks, and S. S. Hodgman, Close-coupled model of Feshbach resonances in ultracold ^{3}He* and ^{4}He* atomic collisions, Phys. Rev. A **104**, 033317 (2021).

[52] L. D. Carr and Y. Castin, Limits of sympathetic cooling of fermions: The role of heat capacity of the coolant, Phys. Rev. A **69**, 043611 (2004).

[53] Assuming the phase-space density of the mixture and the efficiency of the evaporation cycle both remain constant for T greater than T_C the exact functional form is given by $K = \frac{1}{f(\eta)}\left(\frac{S_f(\tau,N_f)}{k_bN_f} + 6\zeta(4)\left(\frac{\bar{\omega}_f}{\bar{\omega}_b}\right)^3\tau\right) - \frac{N_b}{N_f}$ where K is a constant of motion, τ is the reduced temperature, $f(\eta)$ is the average energy of a thermal or condensed boson with energy greater than or equal to ηk_bT, and $\frac{S_f(\tau,N_f)}{k_bN_f}$ is the reduced entropy of a Fermi gas (which is purely a function of τ). The initial assumption essentially fixes K and η, and is hence why we can apply the equation to a range of initial conditions and evaporation heights. The previous equation is only strictly valid for temperatures less than T_C.

[54] H. J. Metcalf and P. Van der Straten, *Laser Cooling and Trapping* (Springer, New York, 1999), Chap. 4, pp. 53–56.

[55] J. Swansson, K. Baldwin, M. Hoogerland, A. Truscott, and S. Buckman, A high flux, liquid-helium cooled source of metastable rare gas atoms, Appl. Phys. B **79**, 485 (2004).

[56] J. Swansson, R. Dall, and A. Truscott, An intense cold beam of metastable helium, Appl. Phys. B **86**, 485 (2007).

[57] B. M. Henson, K. F. Thomas, Z. Mehdi, T. G. Burnett, J. A. Ross, S. S. Hodgman, and A. G. Truscott, Trap frequency

measurement with a pulsed atom laser, Opt. Express **30**, 13252 (2022).

[58] R. C. Hilborn, Einstein coefficients, cross sections, f values, dipole moments, and all that, Am. J. Phys. **50**, 982 (1982).

[59] D. K. Shin, B. M. Henson, R. I. Khakimov, J. A. Ross, C. J. Dedman, S. S. Hodgman, K. G. H. Baldwin, and A. G. Truscott, Widely tunable, narrow linewidth external-cavity gain chip laser for spectroscopy between $1.0 - 1.1\mu$m, Opt. Express **24**, 27403 (2016).

[60] W. Peng, L. Zhou, S. Long, J. Wang, and M. Zhan, Locking laser frequency of up to 40 Ghz offset to a reference with a 10 Ghz electro-optic modulator, Opt. Lett. **39**, 2998 (2014).

[61] K. Harada, T. Aoki, S. Ezure, K. Kato, T. Hayamizu, H. Kawamura, T. Inoue, H. Arikawa, T. Ishikawa, T. Aoki, A. Uchiyama, K. Sakamoto, S. Ito, M. Itoh, S. Ando, A. Hatakeyama, K. Hatanaka, K. Imai, T. Murakami, H. S. Nataraj, Y. Shimizu, T. Sato, T. Wakasa, H. P. Yoshida, and Y. Sakemi, Laser frequency locking with 46 GHz offset using an electro-optic modulator for magneto-optical trapping of francium atoms, Appl. Opt. **55**, 1164 (2016).

[62] D. J. Thompson and R. E. Scholten, Narrow linewidth tunable external cavity diode laser using wide bandwidth filter, Rev. Sci. Instrum. **83**, 023107 (2012).

[63] T. Okoshi, K. Kikuchi, and A. Nakayama, Novel method for high resolution measurement of laser output spectrum, Electron. Lett. **16**, 630 (1980).

[64] A. G. Manning, W. RuGway, S. S. Hodgman, R. G. Dall, K. G. H. Baldwin, and A. G. Truscott, Third-order spatial correlations for ultracold atoms, New J. Phys. **15**, 013042 (2013).

[65] R. G. Dall, A. G. Manning, S. S. Hodgman, W. RuGway, K. V. Kheruntsyan, and A. G. Truscott, Ideal n-body correlations with massive particles, Nat. Phys. **9**, 341 (2013).

[66] S. S. Hodgman, R. I. Khakimov, R. J. Lewis-Swan, A. G. Truscott, and K. V. Kheruntsyan, Solving the Quantum Many-Body Problem via Correlations Measured with a Momentum Microscope, Phys. Rev. Lett. **118**, 240402 (2017).

[67] H. Cayla, C. Carcy, Q. Bouton, R. Chang, G. Carleo, M. Mancini, and D. Clément, Single-atom-resolved probing of lattice gases in momentum space, Phys. Rev. A **97**, 061609(R) (2018).

[68] G. Hercé, C. Carcy, A. Tenart, J.-P. Bureik, A. Dareau, D. Clément, and T. Roscilde, Studying the low-entropy mott transition of bosons in a three-dimensional optical lattice by measuring the full momentum-space density, Phys. Rev. A **104**, L011301 (2021).

[69] C. Carcy, G. Hercé, A. Tenart, T. Roscilde, and D. Clément, Certifying the Adiabatic Preparation of Ultracold Lattice Bosons in the Vicinity of the Mott Transition, Phys. Rev. Lett. **126**, 045301 (2021).

[70] C. Carcy, H. Cayla, A. Tenart, A. Aspect, M. Mancini, and D. Clément, Momentum-Space Atom Correlations in a Mott Insulator, Phys. Rev. X **9**, 041028 (2019).